A&A, 698, A313 (2025)
https://doi.org/10.1051/0004-6361/202554389

Astronomy & Astrophysics

Disentangling the Galactic centre X-ray reflection signal using *XMM-Newton* data

K. Anastasopoulou[1,2,⋆], I. Khabibullin[3,4,5], E. Churazov[4,5], G. Ponti[6,7,8], M. C. Sormani[8],
R. A. Sunyaev[4,5], C. Maitra[7], and S. Piscitelli[6,8]

[1] Center for Astrophysics | Harvard & Smithsonian, 60 Garden Street, Cambridge, MA 02138, USA
[2] INAF-Osservatorio Astronomico di Palermo, Piazza del Parlamento 1, 90134 Palermo, Italy
[3] Universitäts-Sternwarte, Fakultät für Physik, Ludwig-Maximilians Universität, Scheinerstr. 1, 81679 München, Germany
[4] Max Planck Institute for Astrophysics, Karl-Schwarzschild-Str. 1, 85741 Garching, Germany
[5] Space Research Institute (IKI), Profsoyuznaya 84/32, Moscow 117997, Russia
[6] INAF-Osservatorio Astronomico di Brera, Via E. Bianchi 46, 23807 Merate (LC), Italy
[7] Max-Planck-Institut für extraterrestrische Physik, Gießenbachstraße 1, 85748, Garching, Germany
[8] Como Lake Center for Astrophysics (CLAP), DiSAT, Università degli Studi dell'Insubria, via Valleggio 11, 22100 Como, Italy

Received 5 March 2025 / Accepted 2 May 2025

ABSTRACT

Aims. We investigate the X-ray emission from the Galactic centre (GC) region, focusing on the 6.4 keV fluorescent line of neutral or weakly ionised iron, which is commonly attributed to X-ray reflection from dense molecular clouds. Our goal is to separate the reflection signal from other physical X-ray components. We aim to produce a clean map of the 6.4 keV emission, thus providing a better understanding of the X-ray reflection processes in the GC.

Methods. We utilised a deep mosaic of all available *XMM-Newton* observations, encompassing the central 40 square degrees of the Galaxy. This dataset integrates information from 503 individual observations, resulting in a total clean exposure time of 7.5 Ms. The mosaics of two narrow bands centred at 6.7 keV and 6.4 keV, and a broader continuum band at lower energies (5–6.1 keV), provided valuable spatial and spectral information on the X-ray emission. These combined with the stellar mass distribution of our Galaxy enabled us to decompose the observed signal into physically meaningful components.

Results. Our analysis shows that the cleaned 6.4 keV band map, free from the contribution of bright and unresolved point sources, is predominantly shaped by X-ray reflection from dense molecular clouds. The spatial distribution of this emission, which strongly correlates with the molecular gas distribution in the central molecular zone (CMZ), supports the interpretation that this map provides the best estimate of the X-ray reflection signal averaged over the last two decades. This cleaned reflection map could serve as a tool for future studies aiming to quantify upper limits on the reflection contribution from low-energy cosmic rays in unilluminated regions. Moreover, we estimate that, on average, within the CMZ, approximately 65% of the ridge emission contributes to the observed emission in the 6.4 keV band, a factor that should be incorporated into upcoming investigations of the GC, such as polarisation studies of the reflected X-ray continuum from molecular clouds and statistical assessments of the reflection surface brightness.

Key words. ISM: clouds – Galaxy: bulge – Galaxy: center – Galaxy: disk – X-rays: general – X-rays: ISM

1. Introduction

The Galactic centre (GC), the central few degrees of our Galaxy, is an environment of very energetic phenomena (i.e. the flaring activity of Sgr A*, numerous supernova explosions, stellar winds of massive stars, active stars, and various types of X-rays binaries) that result in the emission of soft (<4 keV) as well as hard X-rays (>4 keV; for reviews, see Ponti et al. 2013; Koyama 2018). This environment makes the GC region rich in (apparently) diffuse X-ray emission. In particular, in hard X-rays, two components are commonly invoked to describe the spectral and spatial properties of the emission: the Galactic ridge X-ray emission and the reflected X-ray emission from the massive molecular clouds.

The Galactic ridge X-ray emission has been traced by the ~6.7 keV line, which originates from He-like iron (Fe XXV) and indicates the existence of very hot gas (3–10 keV; e.g. Cooke et al. 1969; Worrall et al. 1982; Koyama et al. 1986, 2007; Yamauchi & Koyama 1993; Revnivtsev et al. 2009). If this hot plasma is bound to compact objects, the spatial distribution of the ridge X-ray emission is expected to follow the smooth distribution of the stellar mass along our Galaxy, including separate contributions of the Galactic disc and bar, the nuclear stellar disc (NSD), and the nuclear star cluster (NSC). Its spectral shape is relatively well established in regions outside the GC and in the hard X-ray band up to ~60 keV (e.g. Krivonos et al. 2007; Yuasa et al. 2012; Krivonos et al. 2025). However, in the very central two degrees of our Galaxy, the origin of the 6.7 keV emission has been widely debated as it was found in excess of what was expected by the stellar mass distribution (SMD) of the Galaxy. This excess emission is attributed to unresolved point sources (a result of a new or larger population of known systems), true hot plasma (due to past activity of Sgr A* or past supernova explosions), or a combination of the two (e.g. Koyama et al. 1989; Yamauchi & Koyama 1993; Muno et al. 2004; Park et al. 2004; Revnivtsev et al. 2007; Uchiyama et al. 2011; Nishiyama et al. 2013; Heard & Warwick 2013). Therefore, in the central few degrees of the Galaxy, the spectrum of the Galactic ridge X-ray emission remains uncertain due to the challenge of disentangling

---

[⋆] Corresponding author:
`konstantina.anastasopoulou@cfa.harvard.edu`

diffuse emission from unresolved point sources and the fact that it likely arises from a spatially variable mixture of populations of point sources (accreting white dwarfs and stars; e.g. Revnivtsev et al. 2006a, 2009; Xu et al. 2016). Anastasopoulou et al. (2023) find that the observed GC X-ray excess might be the result of higher X-ray emissivity per unit stellar mass in the GC, possibly owing to higher metallicity in the GC (e.g. Yamauchi et al. 2016; Feldmeier-Krause et al. 2017; Zhu et al. 2018; Do et al. 2018; Schultheis et al. 2021; Fritz et al. 2021). Anastasopoulou et al. (2023) also find a remarkable similarity between the X-ray emission and the stellar mass density distribution in the GC when scaling for the higher X-ray emissivity in the NSD and NSC, while a small remaining excess in the central 0.3 degrees of the GC can be explained by the contribution of supernova remnants based on the measured supernova rate.

The spectrum of the reflected X-ray emission, dominated by a ~6.4 keV line originating from neutral or weakly ionised iron (Fe Kα), can be readily predicted and indicates the existence of cold gas. However, its spatial distribution is complicated. In the central degrees of the GC, the region known as the central molecular zone (CMZ), the emission from the 6.4 keV line has been found to be asymmetric (in contrast with the more or less uniform distribution of the Galactic ridge X-ray emission) and to be correlated spatially with GC molecular clouds, which are also highly asymmetrically distributed, with approximately three-quarters found at positive longitudes (Bally et al. 1988). The main mechanism of its production is considered to be X-ray reflection off dense molecular clouds, which act as mirrors to the past flaring activity of the central supermassive black hole Sgr A* on timescales of hundreds of years (e.g. Sunyaev et al. 1993; Koyama et al. 1996; Ponti et al. 2013; Churazov et al. 2017a; Khabibullin et al. 2022). Studying the X-ray reflection from molecular clouds in detail has significantly enhanced our understanding of the type and the position of the illuminating source and its variability (e.g. Ponti et al. 2010; Clavel et al. 2013; Terrier et al. 2010; Chuard et al. 2018; Kuznetsova et al. 2022; Stel et al. 2025). In addition to reflection, other mechanisms could account for the observed continuum and the 6.4 keV emission line in the CMZ. One such mechanism is collisional ionisation from accelerated particles (cosmic ray electrons, protons, and ions; e.g. Valinia et al. 2000; Yusef-Zadeh et al. 2002, 2007; Bykov 2002; Dogiel et al. 2009), which was initially proposed to be the case for emission in molecular gas around the Arches cluster as no variability had been observed over an eight-year period (e.g. Wang et al. 2006; Capelli et al. 2011). However, recent studies have shown significant variability around the Arches cluster over a 20-year span, with some residual emission still possibly attributable to cosmic rays (e.g. Clavel et al. 2014; Krivonos et al. 2017; Chernyshov et al. 2018; Kuznetsova et al. 2019; Stel et al. 2025). Observations of fast flux variations in the 6.4 keV-emitting clouds (e.g. Muno et al. 2007; Ponti et al. 2010; Capelli et al. 2012; Clavel et al. 2013; Churazov et al. 2017b; Inui et al. 2009; Terrier et al. 2010; Ryu et al. 2013; Chuard et al. 2018) and polarisation (Churazov et al. 2017a; Marin et al. 2023) are evidence against a cosmic-ray-induced Fe Kα origin, at least for the variable component of the emission (see the review by Ponti et al. 2013).

Several studies have concluded that point sources contribute minimally to the 6.4 keV emission in the GC. For instance, Murakami et al. (2001), using a 100 ks *Chandra* observation of the central 3 × 3.5 arcmin region of the Sgr B2 molecular cloud, resolved approximately 18 sources, which account for only 3% of the luminosity produced by reflection. Moreover, Wang et al. (2002) used *Chandra* data to map the central degrees of the GC, and by extracting composite spectra of the resolved point source population, confirmed that these sources contribute minimally to the 6.4 keV emission. However, they showed that these sources account for most of the observed 6.7 keV emission. On the other hand, very deep ~1 Ms *Chandra* observations of the Galactic ridge and the GC (Revnivtsev et al. 2007, 2009) have shown that a substantial portion of the 4–8 keV energy range is contributed by faint sources. Astrophysical objects like low-mass X-ray binaries and various types of cataclysmic variables are known to produce strong 6.4 keV emission lines, primarily from the inner regions of their accretion discs and reflection from the white dwarf surface (e.g. Kallman & White 1989; Barret et al. 2000).

In this work, we combine spatial and spectral information on the X-ray emission provided by the deep *XMM-Newton* mosaic of the GC and inner Galactic disc region in order to decompose the signal into physically motivated components. Namely, using the spatial correlations of the continuum, the 6.7 keV and 6.4 keV bands, together with the models of the stellar distribution in this region, we derived a ‘residual’ 6.4 keV emission map, which we argue provides the best estimate for the X-ray reflection signal in the GC.

This paper is organised as follows: In Sect. 2 we describe the *XMM-Newton* observations comprising the big mosaic and the SMD models, and in Sect. 3 we present the method we used to produce the clean reflection emission maps. In Sect. 4, we present and discuss our results and compare them with known maps of molecular clouds in the GC. Finally, we provide our conclusions in Sect. 5.

2. Data

2.1. X-ray data

For this project we used all *XMM-Newton* observations available up to 25 February 2024 (503; ~7.5 Ms clean – background flare- and vignetting-corrected – exposure time EPIC-pn equivalent) with exposure times greater than 5 ks and within the central 40 square degrees of our Galaxy. The list of observations is reported in Anastasopoulou et al. (2023), Ponti et al. (2019), and Ponti et al. (2015). The information of the most recent 133 observations are reported in Table A.1.

The calibration and analysis of the observations was performed using the standard tools of the *XMM-Newton* Science Analysis System (SAS) v21.0.0, and is reported in detail in Anastasopoulou et al. (2023). The final product of the analysis is a stray-light free, background subtracted, source excised, and adaptively smoothed mosaic for each *XMM-Newton* detector, and each energy band of interest. The MOS and pn mosaics were combined accounting for the effective area differences between the detectors at the corresponding energy band (details available in the appendix of Anastasopoulou et al. 2023). To isolate the fluorescent Fe K emission from other contaminating processes in the GC, we produced mosaics for three *XMM-Newton* energy bands, 6.3–6.5 keV (X64), 6.62–6.8 keV (X67), and 5.0–6.1 keV (X50). The mosaics in this work are always presented in units of counts per second per pixel (cr/pix), with each pixel measuring 8 × 8 arcseconds. These bands represent the Fe XXV from very hot plasma, the neutral or weakly ionised Fe Kα fluorescent emission, and the continuum at lower energies, respectively. The spectral shape of each component is shown in Fig. 1 where the X67 band is intentionally slightly offset from the 6.7 keV line peak to minimise contamination from the nearby 6.4 keV fluorescent line. The central regions (~8 × 1 degrees) of the raw

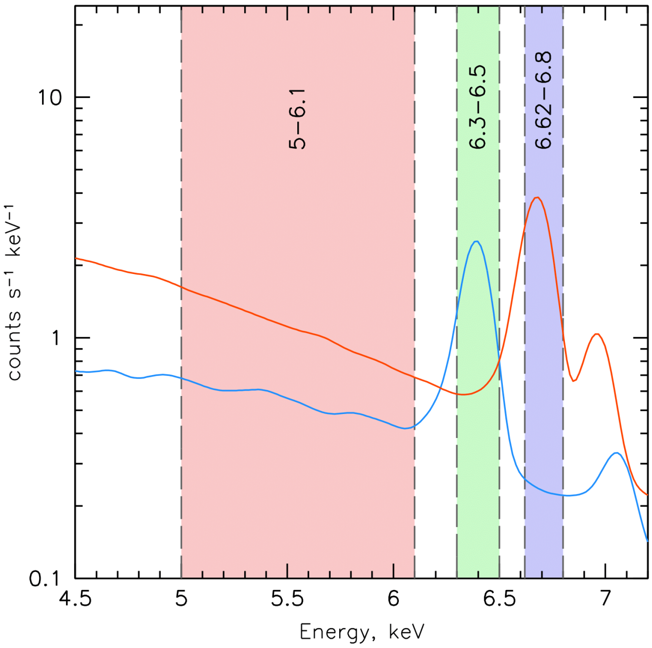

Fig. 1. Spectral representation of the three energy bands used in this project. The bands are highlighted by the shaded regions. The representative model spectra (convolved with the *XMM-Newton* spectra response function) of hot plasma (`apec` model in XSPEC) and reflection (`crefl16` model; Churazov et al. 2017b) are shown as orange and blue lines, respectively.

mosaics at each band are presented in the first three panels of Fig. 2.

2.2. Stellar mass distribution model

The total stellar density of the Milky Way can be represented as a sum of distinct components:

$$\rho_{\rm TOT}(x,y,z) = \rho_{\rm NSC} + \rho_{\rm NSD} + \rho_{\rm BAR} + \rho_{\rm DISC}. \tag{1}$$

These components, arranged by increasing Galactocentric radius R, include:

- The NSC, a dense and slightly flattened structure of stars, surrounding Sgr A* with a mass $\approx 2.5\times10^7\,M_\odot$, dominating within $R \lesssim 10$ pc (Schödel et al. 2014; Neumayer et al. 2020).
- The NSD, a flattened distribution with a mass of approximately $1.05\times10^9\,M_\odot$, prevalent at $10 \lesssim R \lesssim 200$ pc (Launhardt et al. 2002; Sormani et al. 2022b).
- The Galactic bar, an elongated structure in the Galactic plane (GP) with a mass near $1.9\times10^{10}\,M_\odot$, which dominates within $0.2 \lesssim R \lesssim 3$ kpc (Bland-Hawthorn & Gerhard 2016).
- The Galactic disc, which is the main contributor to the stellar mass density beyond $R \gtrsim 3$ kpc.

The SMD model of our Galaxy is created by combining recent models of each individual component. For this project we used the components described as Model 2 in Table 2 and Sect. 2.2 of Anastasopoulou et al. (2023). Namely, for the NSC we used the best-fitting model from Chatzopoulos et al. (2015)[1], for the NSD the fiducial model of Sormani et al. (2022b), for the Galactic bar the bar + long bar from Sormani et al. (2022a), which is based on the numerical models by Portail et al. (2017), and for the Galactic Disc the disc from Sormani et al. (2022a). The SMD model, calculated by integrating the volume density ($\rho(x,y,z)$) along the line of sight to obtain the surface density on the plane of the sky ($\Sigma(l,b)$ where l and b are the Galactic coordinates), is shown in the bottom panel of Fig. 2.

3. Method

The GP is densely populated with many different objects (and classes of objects). It is therefore not surprising that from any location in the GP, we almost always see a composite X-ray spectrum that includes contributions of many unrelated objects along the same line of sight. There are many ways of emphasising one particular component. These range from selecting an energy band, where this component is expected to dominate, to fitting a multi-component spectral model for each sky position. The former is very simple but usually results in a map that can be severely contaminated by other components, while the latter might be too complicated and lead to noisy results if the spectral model is non-linear. One can partially mitigate the noise problem by resorting to linear spectral models (see Churazov et al. 2017b for a two-component case), which works well if the spectral shapes of different components are known. In this case, their normalisations can be independently determined at every position via a linear combination of data. A similar approach can be applied to a collection of maps as is often done in the analysis of cosmic microwave background data (e.g. Planck Collaboration XXII 2016). For a known spectral shape, one can predict the contribution of the component j with amplitude $A_j(x,y)$ to any map i, i.e. $m_i(x,y) = \Sigma_j A_j(x,y)s_{j,i}$. For instance, if $A_j(x,y)$ is a surface density of sources of type j, for example stars, their contribution to the X-ray map $m_i(x,y)$ in the band i is set by the flux $s_{j,i}$ such sources produce in this band. Therefore, knowing $s_{j,i}$ one can select the coefficients α_i so that a linear combination of maps $m(x,y) = \Sigma_i\alpha_i m_i(x,y)$ will eliminate some of the spectral components exactly and preserve the normalisation of the component of interest (at least for the noise-free data). A more practical version of the same procedure is to keep only the requirement of preserving the normalisation of one spectral component and then choose the coefficients so that the resulting map has the smallest L2 norm $\int m^2(x,y)dxdy$. If the component of interest is confined to one particular band, i.e. $s_{0,i} = 0$ for $i \neq 0$, the above procedure reduces to finding the coefficient α_i that minimise the norm:

$$\min_{\alpha} \Sigma_{x,y}\left[\frac{m_0(x,y) - \Sigma_i\alpha_i m_i(x,y)}{\sigma_0(x,y)}\right]^2,$$

where $m_0(x,y)$ is the reference map containing the component of interest (and the contributions of other components too), $\sigma_0^2(x,y)$ is the estimated variance at a given position of the reference map (if it is known and other maps are free from the noise), and $m_i(x,y)$ for $i = 1, N$ are the all other available maps. In this case, the maps need not be X-ray images but could be any images from other bands or models.

The shortcomings and limitations of the above approach are obvious. However, if strong spatial variations of different components are present, this procedure could reveal the level of correlations between the maps and, potentially, clean the maps from some of the contaminating signals. The method we used, compared to equivalent width (EW) approaches, is not biased by regions with low SMD, which can artificially increase the EW due to reduced continuum flux. Our method is less sensitive to variations in the SMD and provides a more accurate representation of the clean 6.4 keV emission, enabling a direct comparison

---

[1] The model by Feldmeier-Krause et al. (2017) estimates a lower total mass for the NSC.

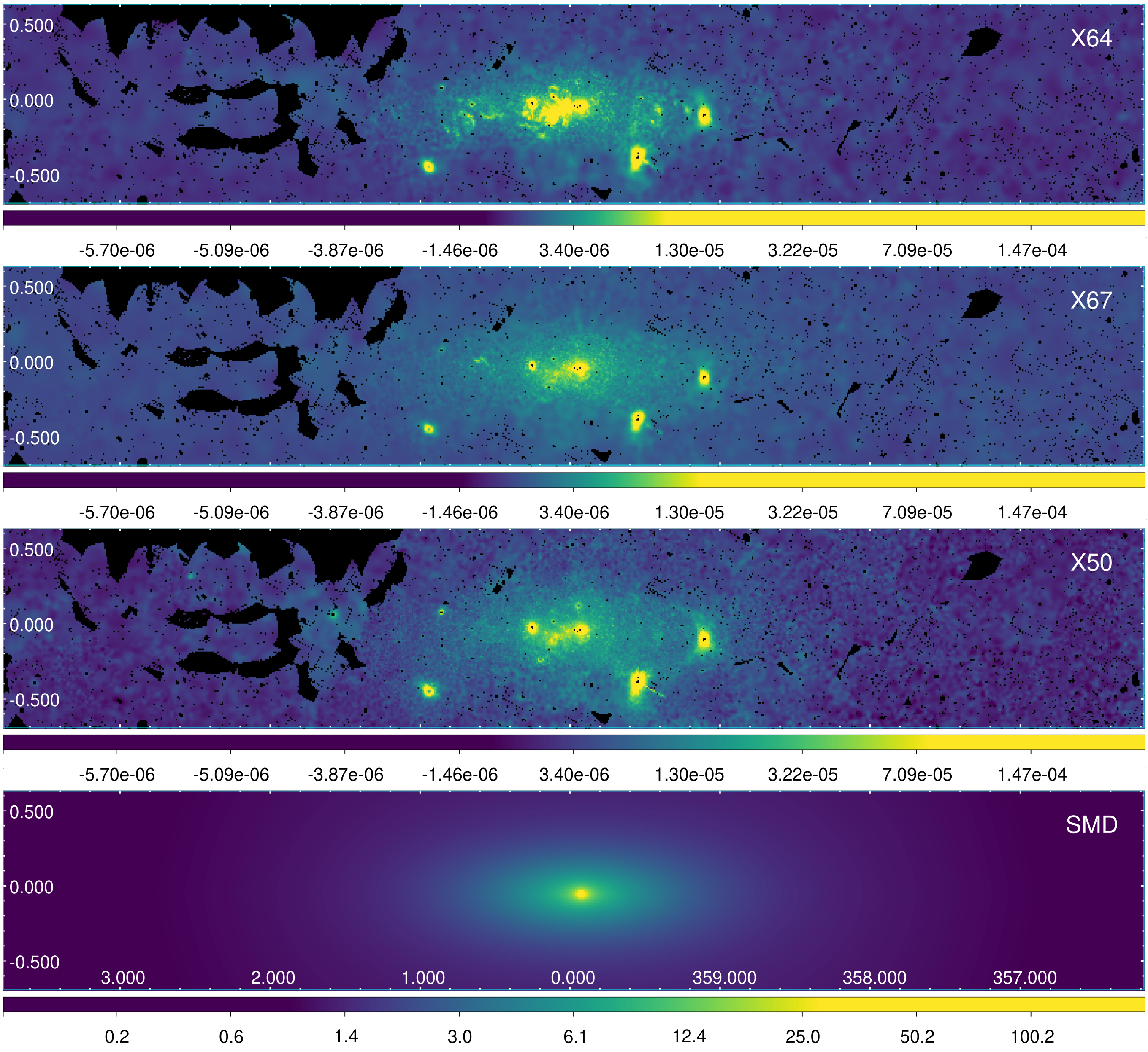

Fig. 2. Raw maps used in this study. From top to bottom: the *XMM-Newton* 6.4 keV (X64), 6.7 keV (X67), the continuum band (X50), and the SMD. The *XMM-Newton* maps are measured in count per second per pixel (cr/pix), whereas the SMD map represents stellar density in 10^3 $M_\odot$/pix. The colour bar ranges are selected arbitrarily to emphasise and display morphological differences. The x-axis and y-axis represent the Galactic longitude and latitude, respectively, in degrees.

with the dense gas distribution in the GC. In what follows we make another simplifying assumption by setting $\sigma_0(x, y) = 1$. Effectively, this means that the algorithm minimises the variance of the residual image after removing the contributions of all components. This is a reasonable choice since we are dealing with smoothed images and mask regions heavily affected by systematics.

Our set of maps, presented in the previous sections, is summarised in Table 1. This study is focused on the X-ray map X64. This map contains the fluorescent line of neutral (or weakly ionised) iron. Other maps serve as possible proxies for various components, which may spatially correlate with our primary maps potentially revealing the origin of the emission (Anastasopoulou et al. 2023). We utilised two distinct maps to represent the SMD across our Galaxy. The first, labelled N, includes contributions from the NSC and the NSD. The second map, labelled B, accounts for contributions from the Galactic bar and the Galactic Disc. These components (N and B) are analysed separately to account for differences in X-ray emissivity between them, as highlighted in Anastasopoulou et al. (2023).

Inclusion and exclusion regions

Our primary goal is to study the origin of the (apparently) diffuse emission by studying its spatial correlation with other components. From this point of view, the emission from bright X-ray sources is the source of contamination. While the bright point sources have already been excluded during the map-making process, some residual traces are present most probably due to dust scattering halos around these sources (e.g. Jin et al. 2017, 2018).

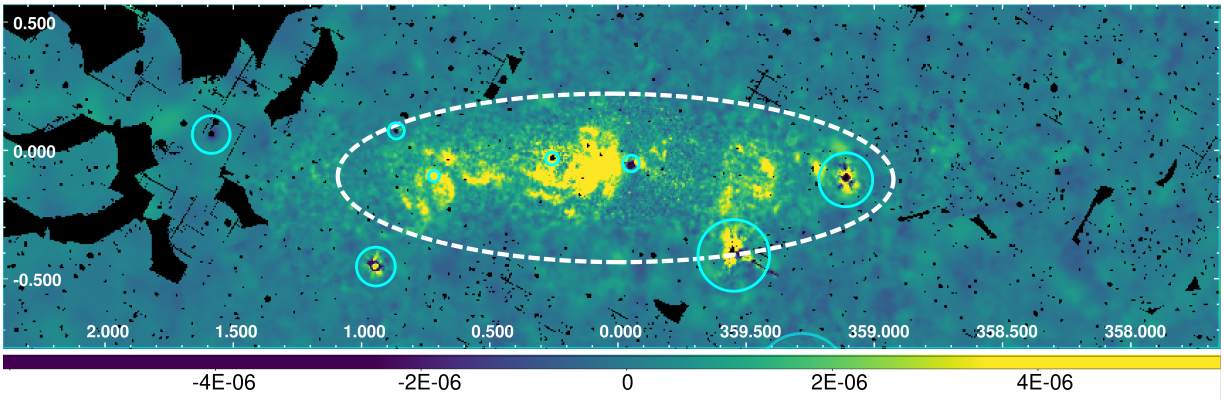

Fig. 3. Example of the cleaned X64 band map (X64 minus C-X67-X50). The mask is shown as a dashed ellipse, and solid circles correspond to bright sources. The map is in units of counts per second per pixel. Black regions indicate areas with no exposure, which may result from the removal of point sources, stray-light artefacts, or chip gaps.

Table 1. Set of maps used in the analysis.

Map	Type	Band
X64 [a]	X-rays	6.30–6.50 keV
X67 [b]	X-rays	6.62–6.80 keV
X50 [c]	X-rays	5.0–6.1 keV
N [d]	Model	Based on kinematic data
B [e]	Model	Based on kinematic data
Const [f]	Model	

Notes. [a]Dominated by 6.4 keV line (proxy to reflected emission). [b]Dominated by 6.7 keV line (proxy to hot plasma). [c]Continuum below the fluorescent line. [d]Projected distribution of stars in the NSC and NSD. [e]Projected distribution of stars in the Galactic bar and Disc. [f]Spatially flat component.

Table 2. Masked regions corresponding to X-ray-bright sources.

Included bright source	ℓ deg	b deg	Radius arcmin
IGR J17252–3616	351.49	–0.37	5.91
multiple	353.56	–0.72	16.69
multiple	354.27	–0.15	15.40
multiple	358.56	–2.21	18.90
1E 1740.7–2942	359.11	–0.11	6.20
SLX 1744–299/300	359.28	–0.89	10.83
2E 1742.9–2929	359.54	–0.41	8.40
Sgr A East	359.94	–0.05	1.92
1E 1743.1–2843	0.26	–0.03	1.49
V* V2606 Oph	0.67	1.18	5.76
CXOGC J174742.4–282227	0.72	–0.10	1.28
multiple	0.81	–2.60	15.63
G0.9+0.1	0.87	0.08	1.88
IGR J17497–2821	0.94	–0.45	4.50
HD 161103	1.39	1.07	14.78
AX J1749.1–2733	1.59	0.06	4.42
multiple	4.78	–0.73	18.81
multiple	5.12	0.65	15.16
multiple	5.25	–0.78	24.78
multiple	5.52	0.64	16.04

For that reason, we applied an additional mask containing a list of regions (Table 2) including bright sources located within these areas. Part of the bright-source mask is shown in Fig. 3 with cyan circles.

Also, as explained in the previous section, the basic assumption is that physically unrelated signals are expected to be spatially uncorrelated. This is likely not true for the GC region, as the density of all classes of sources increases towards the centre of the Milky Way. To partially mitigate this problem, we additionally calculated all correlation coefficients for the entire extent of the map after masking the central region (ellipse shown in Fig. 3) that contains much of the gradient in the surface density of stars or other objects. Masking the central regions is particularly important because most of the molecular clouds that can be sources of ‘reflected’ emission are located there (see Sect. 4.1). In the next sections, we apply this technique to the X64 map obtained by *XMM-Newton*.

4. Results and discussion

4.1. Accounting for different contaminating components

Table 3. Best-fit coefficients.

Set	C $\times10^{-7}$ cr/pix	c_1 $\times10^{-7}$ $\frac{cr/pix}{10^3\ M_\odot/pix}$	c_2 $\times10^{-7}$ $\frac{cr/pix}{10^3\ M_\odot/pix}$	c_3 $\times10^{-1}$	c_4 $\times10^{-1}$
C	3.78	0	0	0	0
C-N	3.21	8.78	0	0	0
C-N-B	1.13	7.15	2.79	0	0
C-N-B-X67-X50	0.53	3.29	0.71	2.08	0.66
*C-X67-X50	0.52	0	0	3.26	0.77

Notes. General model: X64–(C+c_1N+c_2B+c_3X67+c_4X50). We mark the fiducial model with an asterisk. The pixel size is 8 × 8 arcseconds.

Using the method outlined in Sect. 3, we calculated the contributions of all potential components (listed in Table 1) to the X64 map. This analysis is presented for the combined masking of the elliptical central region and bright sources, as it yielded significantly better results compared to using the bright source mask alone, which led to prominent negative residuals (briefly discussed in Appendix B). In Table 3 we present the best-fit coefficients for all possible combinations of the model

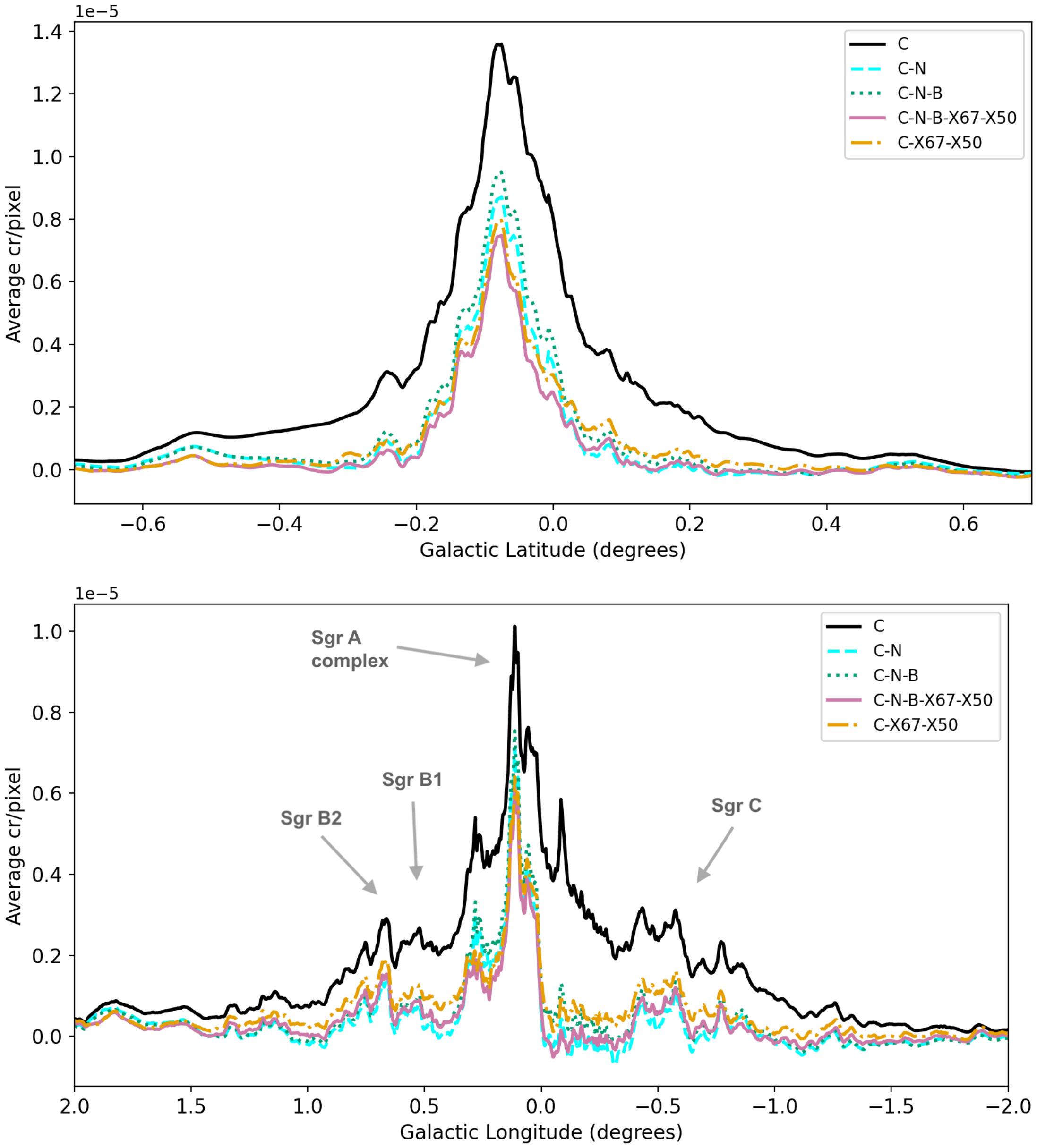

Fig. 4. Latitudinal (top) and longitudinal (bottom) profiles of the X64 cleaned map. The profiles have a width of 0.5 degrees, and the different lines correspond to the different components subtracted from the raw 6.4 keV *XMM-Newton* map.

X64−(C+c_1N+c_2B+c_3X67+c_4X50), and in Table 4 we summarise the different component combinations and the corresponding ratio of the final map variance to the initial map variance for the pixel values across the image. The variance provides a measure of how much noise is reduced after processing the image, such as masking bright sources or regions. However, it is important to note that real astrophysical features, can also contribute to an increase in the variance. Therefore, both noise reduction and the potential contribution of physical structures must be carefully considered when interpreting variance changes.

Overall, we find that the residuals for the C-N-B model are slightly lower than those for the C-N model. The lowest variance results are obtained by removing either the C-X67-X50 or C-N-B-X67-X50 components (Table 4). When we apply the best-fit coefficients to the entire map, we obtain no negative residuals, only slight residuals near very bright sources (Fig. 3).

Table 4. X64 band modelling.

Reference Map (m_0)	Set	$\langle m^2\rangle/\langle m_0^2\rangle$ $\times10^{-1}$
X64	C	3.86
X64	C-N	2.67
X64	C-N-B	2.58
X64	C-N-B-X67-X50	2.02
X64	C-X67-X50	2.13

To quantify further the differences between the various components, we extracted latitudinal and longitudinal profiles from the corresponding maps (Fig. 4). The profiles represent average values within a 0.5-degree width centred on Sgr A*. We present the latitudinal profiles along the central 1.2 degrees and

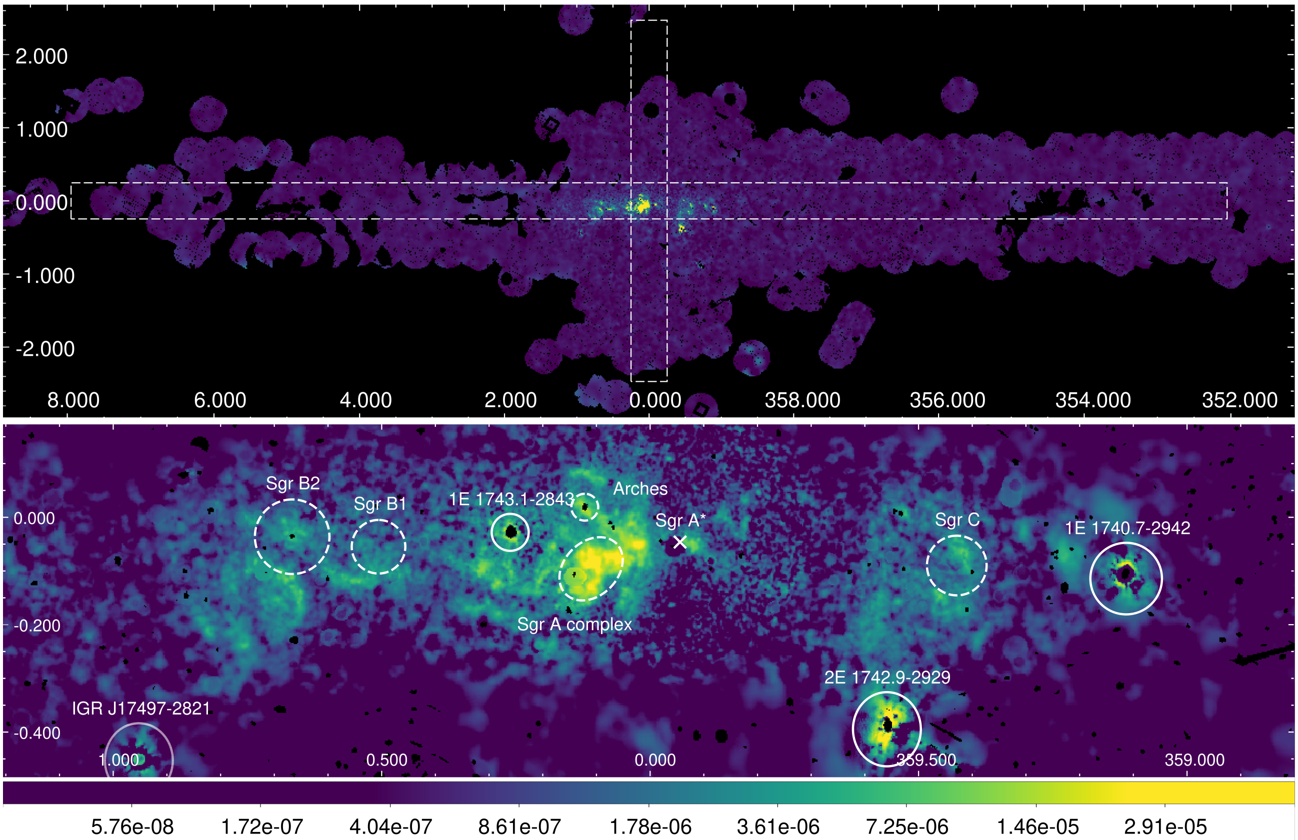

Fig. 5. X64 cleaned full map and zoomed-in view, averaged over ~20 years of *XMM-Newton* observations. Top: X-ray emission across the entire X64 cleaned map representing the reflection. The white rectangular regions indicate the areas used for profile extraction. Bottom: zoomed-in view of the central degrees of the Galaxy, where the reflected emission is concentrated. Bright sources masked out during the analysis are marked with solid white circles, while known molecular clouds are outlined in dashed white. The position of Sgr A* is denoted by an X.

longitudinal profiles along the central 4 degrees. We do not show regions farther from the centre, since there the profiles converge showing emission values close to zero. Regions containing bright sources (listed in Table 2) were masked prior to extracting the profiles. Including these regions resulted in numerous bright peaks, complicating the interpretation of the results. We observe that all models differ slightly, with models C-N and C-N-B-X67-X50 showing slight negative values particularly along the longitudinal profile (bottom panel of Fig. 4). The models with the smaller residual noise are C-N-B-X67-X50 and C-X67-X50. Of the two, we chose C-X67-X50 as the fiducial model since it exhibits no negative residuals.

Model C-N-B, represented by the dotted green line in Fig. 4, has an important application, as the cleaned X64 map is obtained solely by subtracting the SMD model contribution. This allows one to use the best-fit coefficients from Table 3 along with the analytical model in Sect. 2.2 to estimate the ‘non-reflection’ component contributing to the 6.4 keV band. Following Table 3, this component is given by $(1.13 + 7.15\mathrm{N} + 2.79\mathrm{B}) \times 10^{-7}$ cr/pix, where the N component, corresponding to the GC region, yields a 6.3–6.5 keV luminosity[2] per unit stellar mass of $L_X[6.3\text{–}6.5, \mathrm{stellar}] \sim 1.3 \times 10^{26}\,\mathrm{erg\,s^{-1}\,M_\odot^{-1}}$. For comparison, Revnivtsev et al. (2006b) report a 3–20 keV luminosity per stellar mass of $(3.5 \pm 0.5) \times 10^{27}\,\mathrm{erg\,s^{-1}}\,M_\odot^{-1}$, which corresponds to $L_X[6.3\text{–}6.5, \mathrm{apec}] \sim (6 \pm 1) \times 10^{25}\,\mathrm{erg\,s^{-1}}\,M_\odot^{-1}$ for a thermal plasma with $kT \sim 10$ keV. Subtracting this contribution, we estimate the 6.4 keV line luminosity as $L_X[6.3\text{–}6.5, \mathrm{line}] \sim 7 \times 10^{25}\,\mathrm{erg\,s^{-1}}\,M_\odot^{-1}$, corresponding to an EW of ~ 200 eV, consistent with the spectra of cataclysmic variables from which this emission is thought to originate. This could provide valuable insights for future studies such as cosmic ray investigations in the GC. For the C-N-B model, we also observe that the NSC and NSD components (denoted as N) are scaled approximately 2.5 times higher than the bar and Disc components (denoted as B). This behaviour aligns with the finding in Anastasopoulou et al. (2023), that these components require a different scaling to account for the GC X-ray excess (estimated at ~1.9).

4.2. The clean fluorescent map

We present the full *XMM-Newton* mosaic of the X64 map cleaned for contributions of other components (model C-X67-X50) in the top panel of Fig. 5 along with the regions used for profile extraction. We assumed that this map represents a reflected emission coming from dense gas irradiated by X-rays. We note here that this mosaic corresponds to the integrated fluorescent emission over a time period of ~20 years, with observations in the GC and CMZ being deeper and spanning a longer time period than those of the inner GP where the observations are generally shallower (~20 ks) and span a time period of four years. Moreover, different parts of the map were observed at different times. We observe that the reflection emission is concentrated in the central degrees of the GC along the CMZ. We show a zoomed-in view of the central ~2×1 degrees in the

---

[2] We utilised a distance to the GC of 8.2 kpc (GRAVITY Collaboration 2019), an EPIC pn effective area of 460 cm^{-2} , and a mass surface density of $10^3 M_\odot\,\mathrm{pix}^{-1}$.

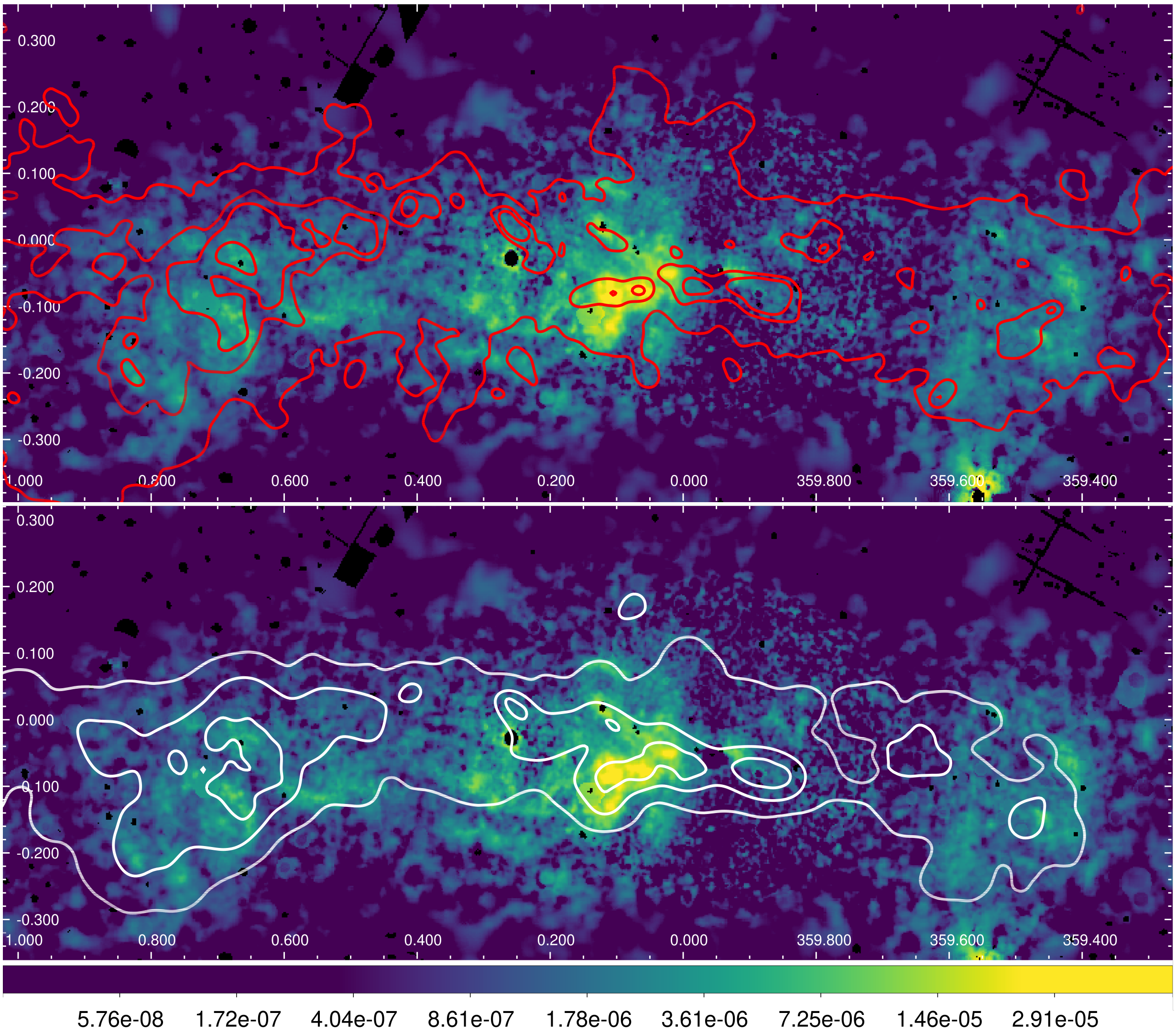

Fig. 6. X64 cleaned map with overlaid contours of the cold and dense molecular gas in the CMZ. Top: *Herschel* SPIRE 250 µm emission contours (Molinari et al. 2011). Bottom: N_2H^+ molecular emission contours (Jones et al. 2012).

bottom panel of Fig. 5. In this panel, bright sources masked out during the fitting process and the profile extraction are indicated by solid white circles. Known molecular cloud positions are outlined with dashed white regions, while the location of Sgr A* is marked by an X. All indicated regions show 6.4 keV emission with particular intensity at the Sgr A molecular complex.

A valuable test to investigate how the cleaned X64 map correlates with reflected emission from molecular clouds is to compare its distribution along the CMZ with tracers of molecular gas. For this purpose, we used contours from two surveys that outline molecular gas emission in the GC. Specifically, we used the *Herschel* SPIRE 250 µm map from the Hi-GAL survey Key Project (Molinari et al. 2010, 2011), which traces a continuous chain of cold and dense clumps, and the N2H$^+$ molecular gas emission map from the Mopra survey of the CMZ (Jones et al. 2012). In Fig. 6, we overlay contours from Molinari et al. (2011) and Jones et al. (2012) on the cleaned X64 map, shown in the top and bottom panels, respectively. This comparison reveals a strong correlation with the distribution of cold and dense clumps as well as the molecular gas, suggesting that this emission indeed arises from X-rays reflected by cold gas in molecular clouds illuminated by past X-ray radiation. Perfect agreement between the distribution of cold gas and the reflected X-ray emission is not expected due to the uneven illumination of the clouds and the different observation times by *XMM-Newton*.

In Fig. 7, we show the fraction of the original (raw) 6.4 keV map that remains after the removal of stars and continuum, plausibly attributed to clean fluorescent emission. We notice that at the position of the most prominent fluorescent features, more than 80% of the raw emission (yellow features) could be attributed to fluorescent emission from molecular gas. Negative regions (shown in black) are present, but of significantly smaller amplitude comparable to the noise level, while areas of the map that do not show reflection remain close to zero (shown in blue). Using the fiducial model, we estimate the non-reflection contribution to the 6.4 keV band, within a central elliptical region consistent to the CMZ (Fig. 3), to a median value of 65%. For regions outside the CMZ the ‘clean reflection’ component approaches zero as is also evident by the latitudinal and longitudinal profiles (Fig. 4). The contribution of the non-reflection component to the CMZ region is significant, and should be considered in future analyses that take into account the pure reflection emission. In addition, the cleaned map can also be used to set upper limits on the 6.4 keV flux from unilluminated

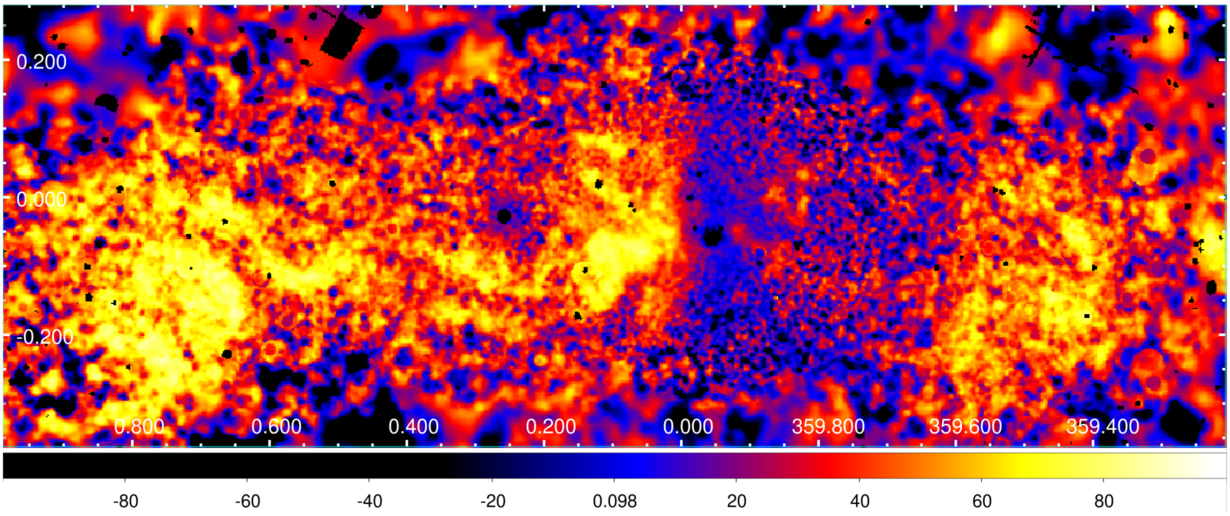

Fig. 7. Fraction of the flux in the X64 band that remains after the best-fitting contributions to this band from stars and continuum have been removed. The remaining flux can plausibly be attributed to the fluorescent emission from molecular gas.

molecular complexes, which is crucial for understanding the low-energy cosmic ray ionisation rate and other steady sources of reflection-like emission.

In this work, we filtered out the contribution of the diffuse component that affects the 6.4 keV band while also correlating with the projected mass distribution. As a key point for future studies, we emphasise that the cleaned X64 map serves as a proxy for the time-averaged reflection emission, which is closely linked to the constant illumination of molecular gas in the CMZ. This illumination could be driven by Sgr A*, cosmic rays, or a multitude of bright X-ray sources in the GC region, each predicting different correlations with molecular gas density. For example, single sources (e.g. Sgr A* or X-ray binaries) would show a distance-dependent trend, cosmic ray models might correlate with gamma-ray emission morphologies, and in the case of multiple X-ray sources, we expect a mix of uniform illumination and a centrally peaked contribution from the NSC.

5. Conclusions

In this work, we utilised mosaics of all available *XMM-Newton* observations of the GC and inner disc, along with SMD models of our Galaxy, to decompose the 6.4 keV line emission into truly reflected emission and contributions from other physical components. Using the spatial correlations of the continuum (X50), 6.7 keV (X67), and 6.4 keV (X64) bands, together with SMD maps, we derived a clean fluorescent X64 map. Key findings include:

- For the 6.30–6.50 keV band (X64), a linear combination of the NSC+NSD and bar+disc maps effectively accounts for much of the diffuse emission that is traced by the distribution of stars. This reveals that outside the CMZ region, most of the 6.4 keV emission can be attributed to unresolved point sources;
- A linear combination of the X67 and X50 maps produces even cleaner maps (in terms of the residual noise in the X64 map). This, on the one hand, confirms that the diffuse continuum emission correlates strongly with the distribution of stars (i.e. Revnivtsev et al. 2007), similar to the NSD and bar components. In addition, using these maps reduces the residuals associated with the brightest compact sources;
- Masking only the bright sources before fitting the maps is insufficient to avoid negative residuals in the final cleaned maps, as the high density of sources in the GC region likely breaks the assumption that physically unrelated signals are spatially uncorrelated, which is essential for using our method. Applying an entire elliptical mask to exclude bright emission in the GC yields optimal results with minimal or no negative residuals, as demonstrated in the Galactic longitudinal and latitudinal profiles;
- Our fiducial clean X64 map reveals that the truly diffuse observed emission is confined to the CMZ region;
- The cleaned map shows a strong correlation with the distribution of molecular gas and the dense and cold gas in the GC. This component likely represents X-rays reflected by cold gas in molecular clouds illuminated by X-rays.

Given that the residual 6.4 keV emission map we derived closely aligns with the distribution of molecular and cold, dense gas along the CMZ, we argue that this map offers the best estimate for the X-ray reflection signal (observed with *XMM-Newton* over the last two decades). Furthermore, we estimate that approximately 65% of the ridge emission contributes to the observed 6.4 keV emission in the CMZ. This contribution should be taken into account in future studies, including polarisation analyses of the reflected X-ray continuum from molecular clouds and statistical examinations of reflection surface brightness fluctuations.

Data availability

The cleaned map presented in Fig. 5 is available at the CDS via anonymous ftp to `cdsarc.cds.unistra.fr` (`130.79.128.5`) or via `https://cdsarc.cds.unistra.fr/viz-bin/cat/J/A+A/698/A313`.

Acknowledgements. KA acknowledges support from *Chandra* grants GO3-24033B, GO0-21010X, and TM9-20001X, and *JWST* grant JWST-GO-01905.002-A. IK acknowledges support by the COMPLEX project from the European Research Council (ERC) under the European Union's Horizon 2020 research and innovation program grant agreement ERC-2019-AdG 882679. MCS acknowledges financial support from the European Research Council under the ERC Starting Grant "GalFlow" (grant 101116226) and from Fondazione Cariplo under the grant ERC attrattività no. 2023-3014. GP acknowledges support from the European Research Council (ERC) under the European Union's Horizon 2020 research and innovation program HotMilk (grant agreement No. 865637), support from Bando per il Finanziamento della Ricerca Fondamentale 2022 dell'Istituto Nazionale di Astrofisica (INAF): GO Large program and from the Framework per l'Attrazione e il Rafforzamento delle Eccellenze (FARE) per la ricerca in Italia (R20L5S39T9). We also made use of NASA's Astrophysics Data System Bibliographic Services.

References

Anastasopoulou, K., Ponti, G., Sormani, M. C., et al. 2023, A&A, 671, A55
Bally, J., Stark, A. A., Wilson, R. W., & Henkel, C. 1988, ApJ, 324, 223
Barret, D., Olive, J. F., Boirin, L., et al. 2000, ApJ, 533, 329
Bland-Hawthorn, J., & Gerhard, O. 2016, ARA&A, 54, 529
Bykov, A. M. 2002, A&A, 390, 327
Capelli, R., Warwick, R. S., Porquet, D., Gillessen, S., & Predehl, P. 2011, A&A, 530, A38
Capelli, R., Warwick, R. S., Porquet, D., Gillessen, S., & Predehl, P. 2012, A&A, 545, A35
Chatzopoulos, S., Fritz, T. K., Gerhard, O., et al. 2015, MNRAS, 447, 948
Chernyshov, D. O., Ko, C. M., Krivonos, R. A., Dogiel, V. A., & Cheng, K. S. 2018, ApJ, 863, 85
Chuard, D., Terrier, R., Goldwurm, A., et al. 2018, A&A, 610, A34
Churazov, E., Khabibullin, I., Ponti, G., & Sunyaev, R. 2017a, MNRAS, 468, 165
Churazov, E., Khabibullin, I., Sunyaev, R., & Ponti, G. 2017b, MNRAS, 465, 45
Clavel, M., Terrier, R., Goldwurm, A., et al. 2013, A&A, 558, A32
Clavel, M., Soldi, S., Terrier, R., et al. 2014, MNRAS, 443, L129
Cooke, B. A., Griffiths, R. E., & Pounds, K. A. 1969, Nature, 224, 134
Do, T., Kerzendorf, W., Konopacky, Q., et al. 2018, ApJ, 855, L5
Dogiel, V., Cheng, K.-S., Chernyshov, D., et al. 2009, PASJ, 61, 901
Feldmeier-Krause, A., Kerzendorf, W., Neumayer, N., et al. 2017, MNRAS, 464, 194
Fritz, T. K., Patrick, L. R., Feldmeier-Krause, A., et al. 2021, A&A, 649, A83
GRAVITY Collaboration (Abuter, R., et al.) 2019, A&A, 625, L10
Heard, V., & Warwick, R. S. 2013, MNRAS, 428, 3462
Inui, T., Koyama, K., Matsumoto, H., & Tsuru, T. G. 2009, PASJ, 61, S241
Jin, C., Ponti, G., Haberl, F., & Smith, R. 2017, MNRAS, 468, 2532
Jin, C., Ponti, G., Haberl, F., Smith, R., & Valencic, L. 2018, MNRAS, 477, 3480
Jones, P. A., Burton, M. G., Cunningham, M. R., et al. 2012, MNRAS, 419, 2961
Kallman, T., & White, N. E. 1989, ApJ, 341, 955
Khabibullin, I., Churazov, E., & Sunyaev, R. 2022, MNRAS, 509, 6068
Koyama, K. 2018, PASJ, 70, R1
Koyama, K., Makishima, K., Tanaka, Y., & Tsunemi, H. 1986, PASJ, 38, 121
Koyama, K., Awaki, H., Kunieda, H., Takano, S., & Tawara, Y. 1989, Nature, 339, 603
Koyama, K., Maeda, Y., Sonobe, T., et al. 1996, PASJ, 48, 249
Koyama, K., Inui, T., Hyodo, Y., et al. 2007, PASJ, 59, 221
Krivonos, R., Revnivtsev, M., Churazov, E., et al. 2007, A&A, 463, 957
Krivonos, R., Clavel, M., Hong, J., et al. 2017, MNRAS, 468, 2822
Krivonos, R., Shtykovskaya, E., & Sazonov, S. 2025, J. High Energy Astrophys., 45, 96
Kuznetsova, E., Krivonos, R., Clavel, M., et al. 2019, MNRAS, 484, 1627
Kuznetsova, E., Krivonos, R., Lutovinov, A., & Clavel, M. 2022, MNRAS, 509, 1605
Launhardt, R., Zylka, R., & Mezger, P. G. 2002, A&A, 384, 112
Marin, F., Churazov, E., Khabibullin, I., et al. 2023, Nature, 7968, 41
Molinari, S., Swinyard, B., Bally, J., et al. 2010, A&A, 518, L100
Molinari, S., Bally, J., Noriega-Crespo, A., et al. 2011, ApJ, 735, L33
Muno, M. P., Baganoff, F. K., Bautz, M. W., et al. 2004, ApJ, 613, 326
Muno, M. P., Baganoff, F. K., Brandt, W. N., Park, S., & Morris, M. R. 2007, ApJ, 656, L69
Murakami, H., Koyama, K., & Maeda, Y. 2001, ApJ, 558, 687
Neumayer, N., Seth, A., & Böker, T. 2020, A&A Rev., 28, 4
Nishiyama, S., Yasui, K., Nagata, T., et al. 2013, ApJ, 769, L28
Park, S., Muno, M. P., Baganoff, F. K., et al. 2004, ApJ, 603, 548
Planck Collaboration XXII. 2016, A&A, 594, A22
Ponti, G., Terrier, R., Goldwurm, A., Belanger, G., & Trap, G. 2010, ApJ, 714, 732
Ponti, G., Morris, M. R., Terrier, R., & Goldwurm, A. 2013, in Cosmic Rays in Star-Forming Environments, eds. D. F. Torres & O. Reimer, Astrophysics and Space Science Proceedings, 34, 331
Ponti, G., Morris, M. R., Terrier, R., et al. 2015, MNRAS, 453, 172
Ponti, G., Hofmann, F., Churazov, E., et al. 2019, Nature, 567, 347
Portail, M., Gerhard, O., Wegg, C., & Ness, M. 2017, MNRAS, 465, 1621
Revnivtsev, M., Molkov, S., & Sazonov, S. 2006a, MNRAS, 373, L11
Revnivtsev, M., Sazonov, S., Gilfanov, M., Churazov, E., & Sunyaev, R. 2006b, A&A, 452, 169
Revnivtsev, M., Vikhlinin, A., & Sazonov, S. 2007, A&A, 473, 857
Revnivtsev, M., Sazonov, S., Churazov, E., et al. 2009, Nature, 458, 1142
Ryu, S. G., Nobukawa, M., Nakashima, S., et al. 2013, PASJ, 65, 33
Schödel, R., Feldmeier, A., Kunneriath, D., et al. 2014, A&A, 566, A47
Schultheis, M., Fritz, T. K., Nandakumar, G., et al. 2021, A&A, 650, A191
Sormani, M. C., Gerhard, O., Portail, M., Vasiliev, E., & Clarke, J. 2022a, MNRAS, 514, L1
Sormani, M. C., Sanders, J. L., Fritz, T. K., et al. 2022b, MNRAS, 512, 1857
Stel, G., Ponti, G., Haardt, F., & Sormani, M. 2025, A&A, 695, A52
Sunyaev, R. A., Markevitch, M., & Pavlinsky, M. 1993, ApJ, 407, 606
Terrier, R., Ponti, G., Bélanger, G., et al. 2010, ApJ, 719, 143
Uchiyama, H., Nobukawa, M., Tsuru, T., Koyama, K., & Matsumoto, H. 2011, PASJ, 63, S903
Valinia, A., Tatischeff, V., Arnaud, K., Ebisawa, K., & Ramaty, R. 2000, ApJ, 543, 733
Wang, Q. D., Gotthelf, E. V., & Lang, C. C. 2002, Nature, 415, 148
Wang, Q. D., Dong, H., & Lang, C. 2006, MNRAS, 371, 38
Worrall, D. M., Marshall, F. E., Boldt, E. A., & Swank, J. H. 1982, ApJ, 255, 111
Xu, X.-j., Wang, Q. D., & Li, X.-D. 2016, ApJ, 818, 136
Yamauchi, S., & Koyama, K. 1993, ApJ, 404, 620
Yamauchi, S., Nobukawa, K. K., Nobukawa, M., Uchiyama, H., & Koyama, K. 2016, PASJ, 68, 59
Yuasa, T., Makishima, K., & Nakazawa, K. 2012, ApJ, 753, 129
Yusef-Zadeh, F., Law, C., & Wardle, M. 2002, ApJ, 568, L121
Yusef-Zadeh, F., Muno, M., Wardle, M., & Lis, D. C. 2007, ApJ, 656, 847
Zhu, Z., Li, Z., & Morris, M. R. 2018, ApJS, 235, 26

Appendix A: Recent *XMM-Newton* observations

Table A.1: *XMM-Newton* observations.

OBSID	Exp pn sec	Exp MOS1 sec	Exp MOS2 sec	clean Exp pn sec	clean Exp MOS1 sec	clean Exp MOS2 sec
0886021101	26137	29746	29688	11100	18086	17766
0886021701	26054	28161	28143	13400	23709	24832
0886031101	28771	31658	31988	7800	22929	26340
0886031601	22746	24592	24586	18155	24614	24586
0886040101	20738	22591	22529	16388	19433	20624
0886040201	20853	22705	22685	16157	20378	21346
0886040301	22032	24608	24599	21534	24556	24599
0886040401	19747	21619	21580	15750	21619	21599
0886040501	24530	29962	29755	12800	17469	18540
0886040601	27769	29933	25319	12641	20017	17255
0886040701	25462	27319	27300	12000	22877	25248
0886061201	19725	21573	21554	3262	9971	12740
0886070301	18520	23575	23505	13626	15182	15847
0886070401	24757	26620	26601	19159	23970	25273
0886070501	19758	20191	19259	19759	20191	19259
0886070601	23480	26620	26583	23480	26464	26497
0886070701	19747	21584	21554	18755	21619	21599
0886070801	28459	30321	30301	24060	28452	28920
0886070901	27684	30006	29999	19457	25651	26827
0886071001	19756	21619	21599	19759	21619	21599
0886071101	24160	26020	26000	24160	26020	26000
0886071201	20550	22408	22386	20553	22418	22399
0886071301	22961	25985	25956	22962	26020	26000
0886080101	24389	29555	29333	16309	22357	23480
0886080201	19759	21619	21599	19762	21619	21599
0886080301	24781	25996	25390	15163	19293	19357
0886080401	18758	20607	20600	18759	20620	20600
0886080501	29530	31612	31601	20060	26007	26373
0886080601	19756	21606	21599	19756	21619	21599
0886080701	29762	31620	31601	29762	31620	31601
0886080801	19761	21619	21599	19762	21619	21599
0886080901	22653	29225	29328	14312	19585	19840
0886081001	24737	26595	26575	9737	17079	19451
0886081101	19762	21619	21599	19762	21619	21599
0886081201	19762	21619	21599	19762	21619	21599
0886081301	20758	22621	22597	20762	22621	22597
0886090201	14295	16522	16500	10200	14141	14276
0886090301	19691	21514	21476	17595	21341	21523
0886090401	19754	21606	21586	16862	21567	21599
0886090501	11260	13109	13099	8760	12797	13099
0886090601	19761	21608	21575	15861	21151	21443
0886090701	8252	10098	10070	6156	10120	10099
0886090801	19755	21592	21583	19655	21608	21599
0886090901	18254	20110	20085	18263	20121	20098
0886091001	8233	10077	10070	8236	10087	10078
0886091101	9271	14813	14721	0	1456	1612
0886091201	8262	10120	10099	8262	10120	10099
0886100101	11762	13608	13598	11462	13619	13598
0886100201	10762	12620	12600	10562	12620	12600
0886100301	8262	10120	10099	8262	10120	10099
0886100401	11947	13792	13798	10656	13485	13642
0886100501	19759	21619	21599	4861	11271	11615
0886100601	16017	19373	19357	0	12685	16812
0886100701	3261	1404	359	3261	1404	359
0886100801	8255	10109	10086	8255	10120	10099
0886100901	8262	10120	10099	8262	10120	10099
0886101001	19754	21619	21583	12059	16211	15827

Table A.1: Continued.

OBSID	Exp pn sec	Exp MOS1 sec	Exp MOS2 sec	clean Exp pn sec	clean Exp MOS1 sec	clean Exp MOS2 sec
0886101201	21241	28559	28551	19760	9669	16097
0886110101	19710	21565	21528	19714	21579	21565
0886110301	19760	21608	21583	15661	21619	21599
0886110401	8262	10120	10099	5962	9513	9683
0886110501	24756	26609	26601	19363	25366	25457
0886110601	19756	20461	19443	14762	20472	19443
0886120901	18850	21598	21599	14052	21502	21495
0886121001	19755	21619	21586	18259	21411	21599
0886121101	8262	10120	10099	7862	10120	10099
0886121201	24647	26620	26598	12900	17936	18694
0886121301	24702	26606	26601	22559	24802	24805
0916790101	13250	15099	15101	2960	8987	10444
0916790201	8262	10106	10088	8262	10120	10099
0916790301	8262	10120	10099	8262	10120	10099
0916790401	8259	10120	10083	8259	10120	10099
0916790501	8262	10120	10099	8262	10120	10099
0916790601	8258	10120	10099	8260	10120	10099
0916790701	8254	10109	10099	8254	10109	10099
0916790801	8256	10120	10099	8262	10120	10099
0916790901	18259	20121	20088	18159	20121	20101
0916791001	8262	10120	10099	8262	9912	9527
0916791101	9161	11019	11001	9061	7069	5957
091679120	18262	10120	10099	0	5762	0
091679130	16407	10120	10099	0	1683	0
0916800201	15059	16900	16900	15060	16908	16900
0916800301	8254	10109	10099	8254	10120	10099
0916800401	8253	10106	10099	8258	10120	10099
0916800501	8252	10112	10073	8255	10120	10099
0916800601	13207	18895	18874	7912	12997	13549
0916800701	9862	11721	11700	9862	11721	11700
0916800801	8262	10120	10099	8262	10120	10099
0916800901	8261	10120	10099	8261	10120	10099
0916801001	8261	10120	10099	8261	10120	10099
0916801101	8262	10120	10099	6262	9758	9915
0916801201	7056	10101	10083	5097	9860	10047
0916801301	7924	18922	18782	2942	5665	5803
0916801401	18255	20110	20101	13859	19705	19944
0916801501	8261	10120	10099	8261	10120	10099
0916810101	8262	10120	10099	8262	10120	10099
0916810201	8262	10120	10099	8262	10120	10099
0916810301	8262	10120	10099	8262	10120	10099
0916810401	8251	10109	10083	8254	10120	10091
0916810501	16741	18587	18585	16746	18601	18585
0916810601	10812	18263	18249	0	7485	8036
0916810701	8262	10120	10099	3862	10120	10099
0916810801	3570	1596	348	3570	1596	348
0916810901	8261	10120	10099	4162	10120	10099
0916811001	2240	2187	2915	2240	2187	2915
0916811201	15880	18871	18850	9600	15493	16304
0916811401	7682	10425	10408	7282	10444	10421
0916811501	13270	18177	18156	7756	10776	10509
0916811701	8251	10109	10086	7953	10120	10099
0916811801	8261	10120	10099	8262	10120	10099
0916811901	9883	13308	13239	4187	8586	8598
0932190101	7659	11011	11001	3258	4002	4159
0932190201	8262	10120	10099	2800	6792	8227
0932190301	8262	10120	10099	3962	8768	9163
0932190401	8261	10120	10099	3961	9860	10099
0932190501	8759	10619	10593	5659	10515	10600
0932190601	9762	11621	11599	9062	11621	11599

Table A.1: Continued.

OBSID	Exp pn sec	Exp MOS1 sec	Exp MOS2 sec	clean Exp pn sec	clean Exp MOS1 sec	clean Exp MOS2 sec
0932190701	9761	11621	11599	9661	11621	11599
0932190801	9752	11599	11588	8954	11621	11599
0932190901	9740	11591	11583	8282	10430	10532
0932191001	7292	10120	10099	7292	10120	10099
0932191101	8262	10120	10099	8262	10120	10099
0932200101	8262	10120	10099	8262	10120	10099
0932200201	8253	10112	10073	8255	10120	10099
0932200301	8259	10120	10099	7359	9964	9891
0932200401	8262	10120	10099	8262	10120	10099
0932200501	8254	10104	10083	8255	10120	10099
0932200601	23063	28850	28923	8198	14505	17604
0932200701	21470	23609	23585	18462	21696	21726
0932200801	19762	21619	21599	19762	21619	21599
0932200901	8262	10120	10099	362	7936	9943
0932201001	7893	10120	10099	1900	9028	9787
0934200101	21300	21650	21646	15711	17567	17090

Appendix B: Limitations of the bright source masking strategy

In this section we present the results obtained when masking only the bright sources. We also explain why this strategy does not perform as well as masking in addition, the entire central region affected by reflection using an elliptical mask. The latter is the approach adopted in our main analysis (Sect. 4.1; Fig. 3).

The cleaned map (Fig. B.1) using only the bright source mask shows significant negative residuals when minimising the variance across the entire map — particularly in the GC near Sgr A* and around bright sources. This likely happens since both the peak of the reflected emission and the thermal emission are concentrated in the GC. Hence, some of the reflected emission is removed. This is further reflected in the Galactic longitudinal profiles. When using the bright source mask (Fig. B.2), all models show significant negative residuals particularly close to the GC. When comparing these results to those obtained with elliptical masking (Figs. 3 and 4), the improved performance of the adopted method, with almost no negative residuals, becomes evident.

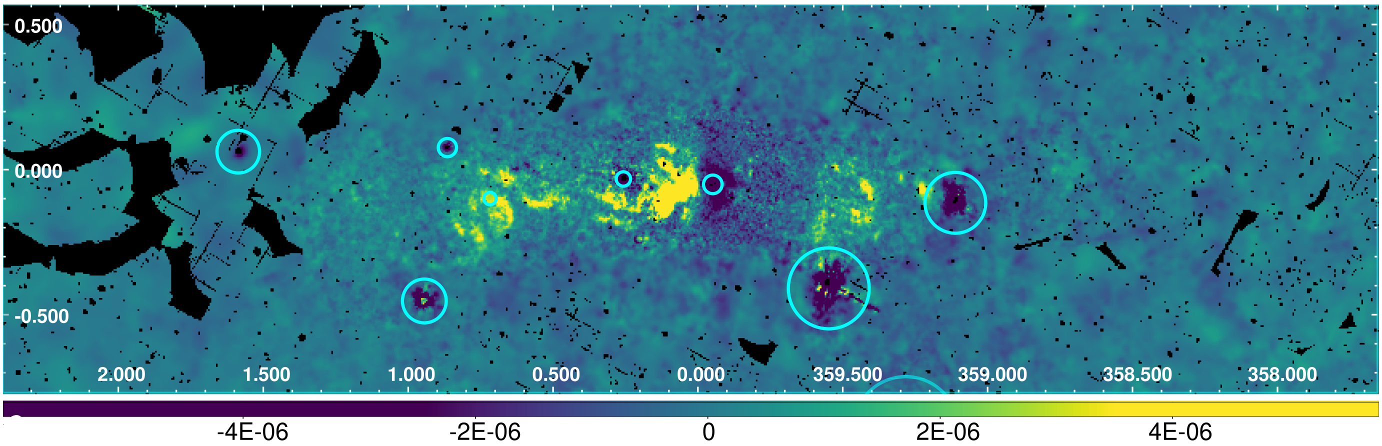

Fig. B.1. Example of the cleaned X64 band maps (X64 minus C-X67-X50) when masking only for bright sources. The mask is shown with the cyan circles. Significant negative residuals remain at the GC near Sgr A* and near the bight sources.

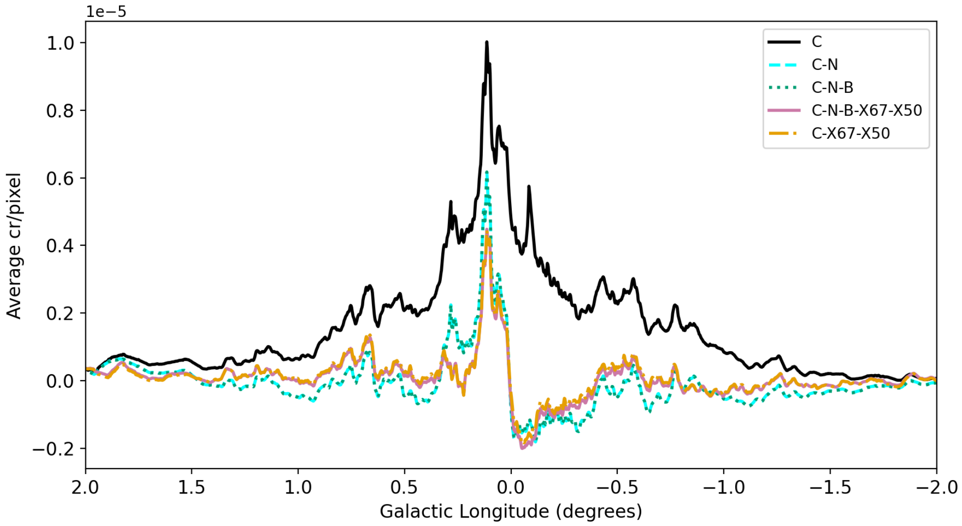

Fig. B.2. Longitudinal profiles of the X64 cleaned map when masking only for bright sources. Significant negative residuals remain, particularly at the GC near Sgr A*.